

Article

# Influence of $\text{HB}_2\text{Nb}_3\text{O}_{10}$ -Based Nanosheet Photocatalysts (B = Ca, Sr) Preparation Method on Hydrogen Production Efficiency

Sergei A. Kurnosenko , Vladimir V. Voytovich , Oleg I. Silyukov \* , Ivan A. Rodionov ,  
Ekaterina N. Malygina and Irina A. Zvereva 

Department of Chemical Thermodynamics and Kinetics, Institute of Chemistry, Saint Petersburg State University, Saint Petersburg 198504, Russia

\* Correspondence: oleg.silyukov@spbu.ru

**Abstract:** Photocatalytic activity of  $\text{HB}_2\text{Nb}_3\text{O}_{10}$  perovskite nanosheets (B = Ca, Sr) has been systematically investigated in the reactions of hydrogen production, depending on the method of the photocatalyst preparation: using the pristine nanosheets in the parent suspension without reassembly, filtered nanosheets as well as nanosheets restacked by hydrochloric acid. Photocatalytic measurements were organized in such a way as to control a wide range of parameters, including the hydrogen generation rate, quantum efficiency of the reaction, potential dark activity of the sample as well as stability and pH of the reaction suspension. Exfoliation of the niobates into nanosheets allowed obtaining efficient photocatalysts surpassing the initial bulk materials in the activity up to 55 times and providing apparent quantum efficiency up to 20.8% after surface decoration with a Pt cocatalyst. Among the reassembled samples, greater hydrogen evolution activity was exhibited by simply filtered nanosheets that, unlike the HCl-restacked ones, were found to possess much lower specific surface area in a dry state but contain a perceptible amount of tetrabutylammonium cations on the surface. The activity difference, potentially, is associated with the fact that the filtered nanosheets undergo ultrasonic disaggregation before photocatalytic tests much easier than their HCl-restacked counterparts and, thanks to this, have greater active surface in the reaction suspension. In addition, the enhanced activity of the filtered nanosheets may be due to the presence of tetrabutylammonium as an organic modifier on their surface, which is consistent with the high photocatalytic performance of organically modified layered perovskites considered in our previous reports.

**Keywords:** photocatalysis; hydrogen; layered perovskite; niobate; nanosheets; exfoliation; reassembly

**Citation:** Kurnosenko, S.A.; Voytovich, V.V.; Silyukov, O.I.; Rodionov, I.A.; Malygina, E.N.; Zvereva, I.A. Influence of  $\text{HB}_2\text{Nb}_3\text{O}_{10}$ -Based Nanosheet Photocatalysts (B = Ca, Sr) Preparation Method on Hydrogen Production Efficiency. *Catalysts* **2023**, *13*, 614. <https://doi.org/10.3390/catal13030614>

Academic Editors: Concetta Ruocco and Marco Martino

Received: 30 January 2023

Revised: 10 March 2023

Accepted: 13 March 2023

Published: 18 March 2023



**Copyright:** © 2023 by the authors. Licensee MDPI, Basel, Switzerland. This article is an open access article distributed under the terms and conditions of the Creative Commons Attribution (CC BY) license (<https://creativecommons.org/licenses/by/4.0/>).

## 1. Introduction

Ion-exchangeable layered perovskite-like oxides are solid crystalline compounds with a block-type structure, which can be represented as an alternation of negatively charged slabs of corner-shared perovskite octahedra and interlayer spaces populated by alkali cations. According to structural features, ion-exchangeable layered perovskites may be classified into two groups: the Dion–Jacobson phases and the Ruddlesden–Popper phases, corresponding to general formulae  $A'[A_{n-1}B_nO_{3n+1}]$  and  $A'_2[A_{n-1}B_nO_{3n+1}]$ , respectively ( $A'$  = alkali cation,  $A$  = alkaline earth or transition cation,  $B$  = Nb, Ta, Ti, etc.) [1–3].

A unique feature of layered materials is the possibility of their exfoliation into separate nanosheets (or differently called—nanolayers) to obtain catalytic materials with a high specific surface area and nanoscale properties [4,5]. In the case of layered perovskite-like oxides, the ability to undergo exfoliation into nanosheets is most typical of the so-called protonated forms, which can be obtained by replacing interlayer alkali cations with protons in acidic aqueous solutions [6]. The exfoliation process, as a rule, occurs by introducing bulk organic cations into the interlayer space (tetrabutylammonium hydroxide TBAOH is most often used), followed by swelling with solvent molecules and, as a result, increasing the

distance between individual layers up to complete separation under any physical impact (shaking or sonication) [7,8]. In the context of photocatalysis, the exfoliation leads to a decrease in the specific volume of particles in favor of their surface, which shortens the charge migration path and, thus, minimizes the undesirable effect of volume electron-hole recombination on photocatalytic performance. Moreover, the exfoliation into nanosheets usually affects the bandgap energy of the photocatalyst. As a result, many layered oxides after exfoliation show a significantly higher activity in photocatalytic reactions than their bulk analogues [9–12]. In addition, the nanosheets can serve as components of nanostructured composite photocatalysts being prepared by coprecipitation with other nanoparticles, layer-by-layer deposition or electrostatic self-assembly [13–21].

A number of layered perovskite-like oxides with the general formula  $A'[A_{n-1}B_nO_{3n+1}]$  ( $A' = \text{Li, Na, K, Rb, Cs}$ ;  $B = \text{Ca, Sr, Ba, Pb}$ ), belonging to the Dion-Jacobson phases, have been actively investigated since the compounds of the composition  $A'\text{Ca}_2\text{Nb}_3\text{O}_{10}$  were first obtained [22]. The most well studied among them is the  $\text{KCa}_2\text{Nb}_3\text{O}_{10}$  oxide, whose structure consists of two-dimensional perovskite layers of  $\text{NbO}_6$  octahedra, alternating with  $\text{K}^+$  ions, and  $\text{Ca}^{2+}$  ions occupying 12-coordinated positions in the center of perovskite blocks [23].  $A'\text{B}_2\text{Nb}_3\text{O}_{10}$  oxides can be converted into their protonated forms  $\text{HB}_2\text{Nb}_3\text{O}_{10} \cdot y\text{H}_2\text{O}$  via the ion exchange in acids [6]. These protonated and hydrated oxides have attracted great attention due to the capability of intercalating amines [24], grafting alcohols [25] and exfoliating into nanosheets with the perovskite structure via the insertion of bulky organic bases [7,8]. Protonated forms, organically modified derivatives and nanosheets of the  $A'\text{B}_2\text{Nb}_3\text{O}_{10}$  niobates as well as composite materials on their basis have already proven to be efficient photocatalysts of hydrogen generation [26–31]. In particular, reassembled nanosheets of  $\text{HB}_2\text{Nb}_3\text{O}_{10}$  ( $B = \text{Ca, Sr}$ ) niobates outperform their bulk precursors in terms of the activity by two- to four-times [9,12]. After surface modification with a Pt cocatalyst, they demonstrate a hydrogen generation rate up to  $900 \mu\text{mol} \cdot \text{h}^{-1} \cdot \text{g}^{-1}$  from aqueous isopropanol [10] and up to  $530 \mu\text{mol} \cdot \text{h}^{-1} \cdot \text{g}^{-1}$  from aqueous triethanolamine [12], respectively (300 W xenon lamp). The use of methanol as a sacrificial agent allows reaching much greater activity up to  $9000 \mu\text{mol} \cdot \text{h}^{-1} \cdot \text{g}^{-1}$  (500 W xenon lamp) [9]. To improve the photocatalytic performance and expand the light absorption range, the perovskite nanosheets have been used to yield a wide range of composite materials with  $g\text{-C}_3\text{N}_4$  [32],  $\text{CdS}$  [14,17,20],  $\text{Co}_x\text{P}$  [33,34],  $\text{CaNb}_2\text{O}_6$  [18], graphene oxide [19], ruthenium complexes [35–37] and other modifiers. Most nanosheet-based photocatalysts were shown to retain their activity for several running cycles [12,17,19,20,32,38] or, at least, preserve 80–90% of the initial performance [33,34]. However, many studies do not provide quantum yields or efficiencies and do not compare the activity of the composites obtained with that of the initial nanosheets under the same conditions, which hinders the analysis of the available data.

One of important issues in the study of nanosheet-based photocatalysts is the method for isolating nanosheets after liquid-phase exfoliation. Basically, they may be used either in the as-prepared parent suspensions or after reassembly and redispersing in the reaction solution. Obviously, the specific approach used (filtering, precipitation by electrolytes, ultracentrifugation, etc.) should have a significant impact on photocatalytic activity. The vast majority of studies involve the addition of salts [13,15,16,19,33,34], acids [12,14,18,20,21,34–38] or alkalis [9]. This approach is very convenient in practice and allows one to rapidly precipitate suspended particles, dry them and subsequently use as conventional powder photocatalysts. However, the alternative approaches are rarely applied and the available literature does not cover the relationship between the form of perovskite nanosheets used and their photocatalytic performance. In view of this, the present paper aims to compare the hydrogen evolution activity of pristine  $\text{HB}_2\text{Nb}_3\text{O}_{10}$  ( $B = \text{Ca, Sr}$ ) nanosheets without reassembly, filtered nanosheets and nanosheets precipitated via the suspension acidification as well as to consider potential reasons for the differences in their photocatalytic behavior.

Here and below, the protonated niobates are abbreviated as HBN<sub>3</sub> (HCN<sub>3</sub> for B = Ca and HSN<sub>3</sub> for B = Sr) and three aforementioned forms of their nanosheets are designated as HBN<sub>3</sub> NSs, HBN<sub>3</sub> filtered NSs and HBN<sub>3</sub> HCl-restacked NSs, respectively.

## 2. Results and Discussion

### 2.1. Characterization of Protonated Niobates and Their Nanosheets

Suspensions of the HBN<sub>3</sub> NSs were successfully prepared via the physical-chemical exfoliation of the protonated niobates in aqueous TBAOH. Approximate concentrations of HCN<sub>3</sub> and HSN<sub>3</sub> NSs in the final suspensions were revealed to be 500 and 950 mg/L, respectively. The corresponding exfoliation yields were ~50% and ~75% from the theoretically possible amounts (1025 mg/L for HCN<sub>3</sub> NSs and 1250 mg/L for HSN<sub>3</sub> NSs). Both types of reassembled nanosheets (filtered NSs and HCl-restacked NSs) were also collected. From a preparative point of view, the precipitation of nanosheets by hydrochloric acid proved to be a much more convenient approach compared to the simple filtering. In the first case, the flocculent sediment practically does not clog the filter pores and a filtration rate remains consistently high. In the second case, the pores quickly become clogged with nanosheets and the filtration rate drops sharply at the very beginning of the procedure. The practical yield of the reassembly was approximately 60–70% for HBN<sub>3</sub> filtered NSs and 85–95% for HCl-restacked NSs.

The protonated niobates and their reassembled nanosheets were preliminarily studied by XRD analysis (Figure 1). The patterns of both HBN<sub>3</sub> precursors correspond to those from the ICDD database (cards №00-039-0915 and №00-051-1878, shown as dashes) indicating that the samples are single-phase and do not contain detectable amounts of crystalline impurities. The patterns were successfully indexed in the tetragonal system and the lattice parameters calculated (Table 1) were found to be consistent with the literature data [6,39]. XRD analysis of the reassembled nanosheets clearly indicates the preservation of the layered perovskite structure although their patterns are not completely identical to those of the protonated precursors. One of the main differences is strong broadening of the diffraction peaks pointing to a stacking disorder of perovskite layers arisen during the reassembly, which is especially pronounced in the case of HCl-restacked NSs. Another difference observed for HBN<sub>3</sub> filtered NSs is a low-angle shift of (00*x*) reflections (which refer to planes parallel to the layered oxide layers) corresponding to a greater *c* lattice parameter being equal to the interlayer distance *d* (defined as a distance between the centers of adjacent perovskite layers) (Table 1). At the same time, the *c* parameter of HCl-restacked NSs is approximately equal to that of the protonated niobate. Consequently, there exist some factors preventing the tight closure of the nanosheets being filtered without the suspension acidification. For instance, this may be the influence of adsorbed TBA<sup>+</sup> cations and/or more pronounced embedding water molecules between the perovskite nanosheets being reassembled.

**Table 1.** Lattice parameters in the tetragonal system, interlayer distances, light absorption edges, specific surface areas of the protonated niobates and their reassembled nanosheets as well as hydrodynamic radii and ζ-potentials of the pristine nanosheets in suspensions before reassembly.

Sample	<i>a</i> , Å	<i>c</i> = <i>d</i> , Å	E <sub>g</sub> , eV	λ <sub>max</sub> , nm	S, m <sup>2</sup> /g	R <sub>h</sub> , nm	ζ, mV
HCN <sub>3</sub>	3.82	16.0	3.50	354	7.6	–	–
HCN <sub>3</sub> NSs	–	–	–	–	–	86, 19	–26.5
HCN <sub>3</sub> filtered NSs	~3.8	~17	3.42	363	17.7	–	–
HCN <sub>3</sub> HCl-restacked NSs	~3.8	~16	3.38	367	76.3	–	–
HSN <sub>3</sub>	3.89	16.4	3.26	380	3.1	–	–
HSN <sub>3</sub> NSs	–	–	–	–	–	47	–24.0
HSN <sub>3</sub> filtered NSs	~3.9	~17	3.14	395	10.0	–	–
HSN <sub>3</sub> HCl-restacked NSs	~3.9	~17	3.26	380	103	–	–

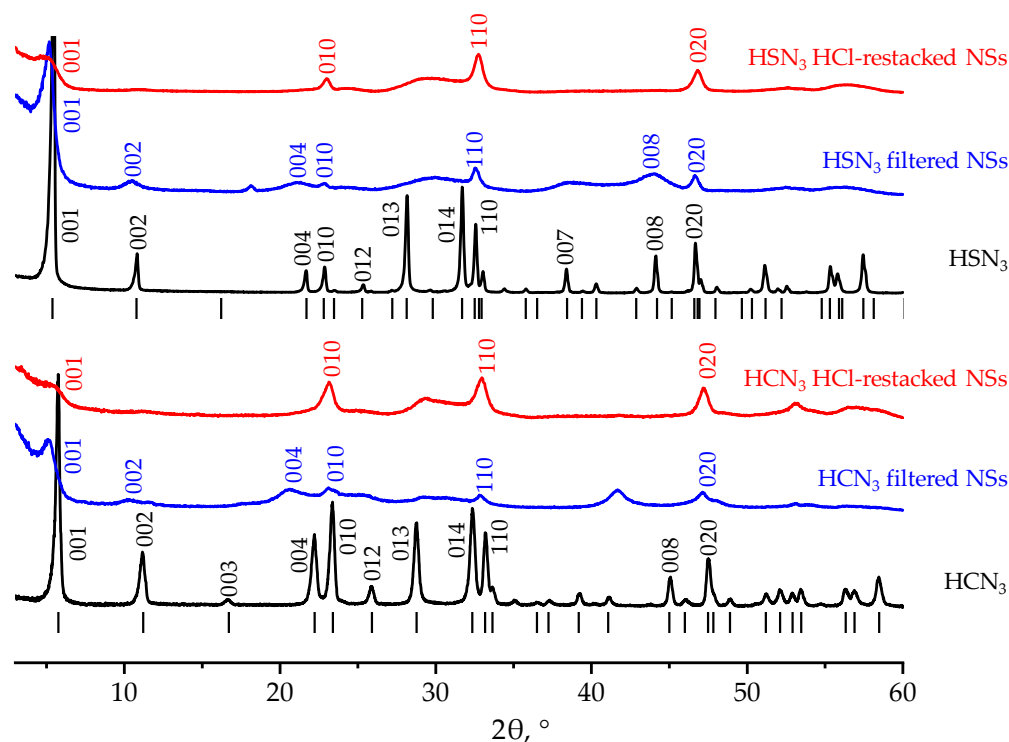


**Figure 1.** Powder XRD patterns of the protonated niobates and their reassembled nanosheets.

Raman spectra of the reassembled nanosheets preserve all of the main vibrational modes related to the layered perovskite-like lattice of the niobates under study (Figure 2). At the same time, the symmetric stretching frequency of axial Nb–O bonds decreases by  $15\text{--}20\text{ cm}^{-1}$ . The shift of this band is quite expected upon a variety of transformations involving the interlayer space (including exfoliation) since interlayer surrounding of the oxygens inevitably changes affecting the O–Nb–O vibrations. Moreover, the Raman spectra clearly show the presence of residual tetrabutylammonium in the samples of HBN<sub>3</sub> filtered NSs: one can observe the bands of C–N ( $1035\text{ cm}^{-1}$ ), C–C ( $1060\text{ cm}^{-1}$ ) and C–H ( $2820\text{--}3050\text{ cm}^{-1}$ ) stretching, C–C–H ( $1130\text{ cm}^{-1}$ ) and C–N–C ( $1450\text{ cm}^{-1}$ ) bending as well as CH<sub>2</sub> wagging ( $1320$  and  $1450\text{ cm}^{-1}$ ). Apparently, the TBA<sup>+</sup> cations strongly associate with the niobate nanosheets and cannot be removed completely even after their thorough rinsing with an excess of water. However, the tetrabutylammonium vibration bands are barely visible in the case of the HCl-restacked NSs and can be seen only after the spectrum upscaling by several times (Figure 2). Even after this, the organics bands remain relatively weak: their intensity does not exceed that of the bands related to hydroxy groups ( $3000\text{--}3600\text{ cm}^{-1}$ ) and water molecules ( $1620\text{ cm}^{-1}$ ), which are known to be weak Raman scatterers. Consequently, the residual tetrabutylammonium content in the HCl-restacked NSs should be much lower than in the filtered NSs.

To verify the latter assumption, the reassembled nanosheets were investigated by means of TG and elemental CHN-analysis. Their TG curves are quite different from those of the protonated precursors (Figure S1), which exhibit two well distinguishable mass loss stages related to the deintercalation of interlayer water molecules ( $30\text{--}100\text{ }^{\circ}\text{C}$ ) and further decomposition of the anhydrous protonated niobate ( $275\text{--}500\text{ }^{\circ}\text{C}$ ). The nanosheets, on the contrary, demonstrate a generally gradual mass loss in the temperature range below  $500\text{--}600\text{ }^{\circ}\text{C}$ , which is difficult to divide into subsections. Such a behavior of the reassembled nanosheets, apparently, is consistent with their disordered nature observed from the XRD data. However, the total mass loss of the HCN<sub>3</sub> filtered NSs is 3.6% more than that of the HCN<sub>3</sub> HCl-restacked NSs, which points to a probably greater amount of the residual tetrabutylammonium in the former. This fact is clearly proved by the following quantitative compositions calculated from the CHN and TG

data: HCN<sub>3</sub> filtered NSs (H<sub>0.82</sub>Ca<sub>2</sub>Nb<sub>3</sub>O<sub>10</sub>·0.18TBA·0.75H<sub>2</sub>O), HCN<sub>3</sub> HCl-restacked NSs (H<sub>0.99</sub>Ca<sub>2</sub>Nb<sub>3</sub>O<sub>10</sub>·0.01TBA·1.6H<sub>2</sub>O), HSN<sub>3</sub> filtered NSs (H<sub>0.84</sub>Sr<sub>2</sub>Nb<sub>3</sub>O<sub>10</sub>·0.16TBA·1.65H<sub>2</sub>O) and HSN<sub>3</sub> HCl-restacked NSs (H<sub>0.97</sub>Sr<sub>2</sub>Nb<sub>3</sub>O<sub>10</sub>·0.03TBA·1.70H<sub>2</sub>O). These results are in good agreement with the differences in the tetrabutylammonium bands' intensity in the Raman spectra considered above (Figure 2) and confirm our assumption concerning the organic content in the reassembled samples. Thus, the HBN<sub>3</sub> filtered NSs, strictly speaking, represent some sort of hybrid inorganic-organic materials, not just oxide particles, with the TBA<sup>+</sup> cations strongly bound to the surface. The HBN<sub>3</sub> HCl-restacked NSs, on the contrary, contain only trace amounts of tetrabutylammonium that, apparently, is easily washed out of the sample in the form of tetrabutylammonium chloride after the suspension acidification.

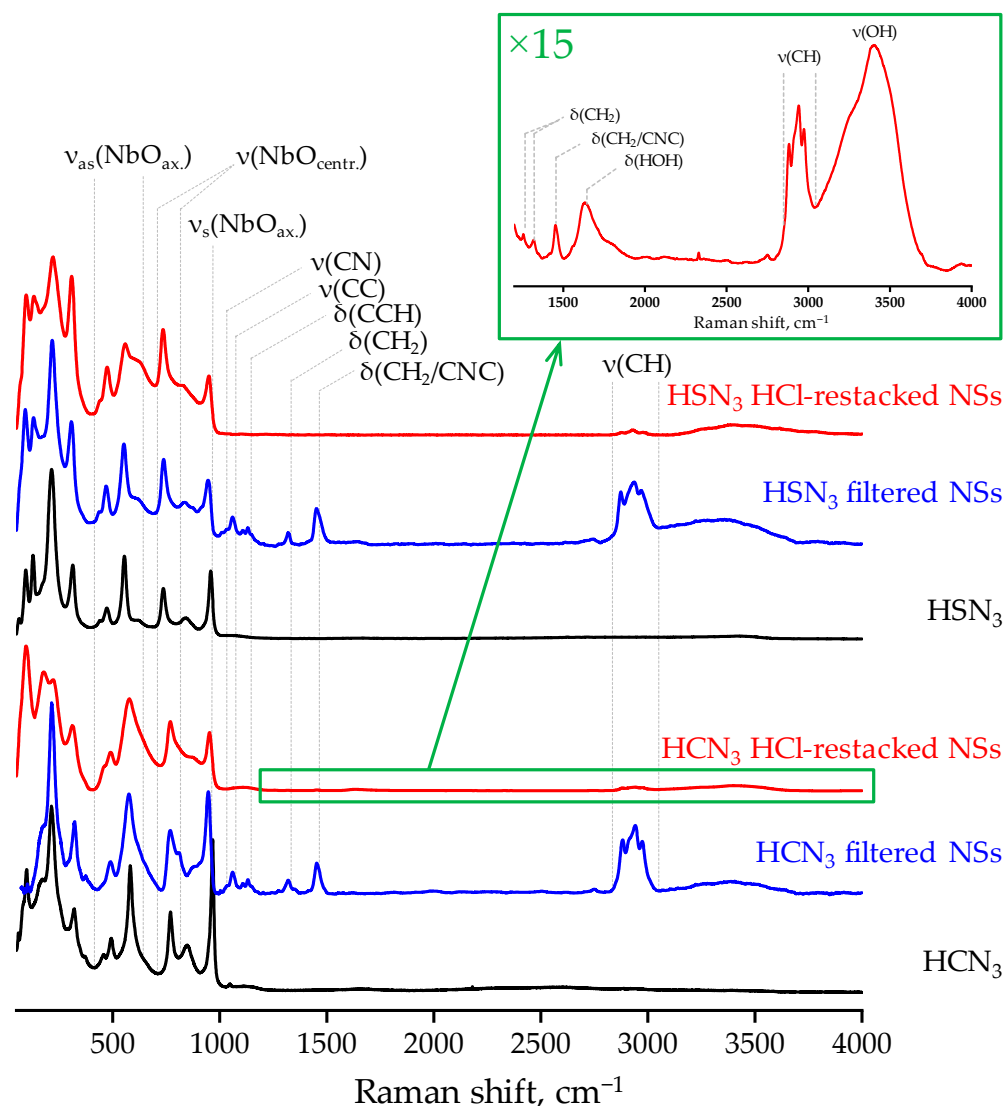


**Figure 2.** Raman spectra of the protonated niobates and their reassembled nanosheets.

Exfoliated and reassembled niobates, with the exception of HSN<sub>3</sub> HCl-restacked NSs, demonstrate lower bandgap energy values than their bulk precursors (Figure 3, Table 1), which allows the final nanosheets to utilize a greater part of light to drive a photocatalytic reaction. Particularly, the absorption edge of HSN<sub>3</sub> filtered NSs approaches very close to the visible spectrum region ( $E_g = 3.14$  eV,  $\lambda_{max} = 395$  nm). However, while HCN<sub>3</sub> HCl-restacked NSs possess even lower bandgap energy than filtered NSs, its value for HSN<sub>3</sub> HCl-restacked NSs is equal to that for the protonated niobate. A specific reason for this difference is yet unclear, however, it may originate from the peculiarities of the nanosheet stacking upon the acid treatment.

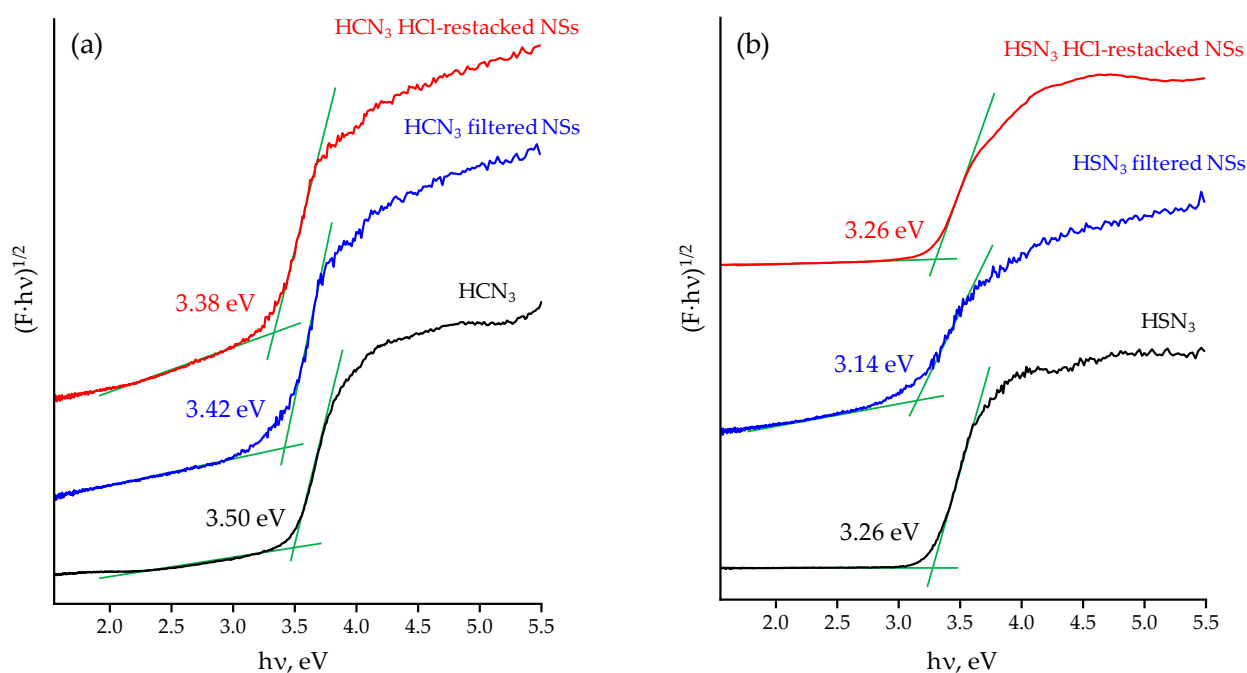


**Figure 3.** Tauc plots for the protonated forms and reassembled nanosheets of HCN<sub>3</sub> (a) and HSN<sub>3</sub> (b) niobates.

The morphology of the pristine HBN<sub>3</sub> NSs was investigated by means of TEM (Figure S2). Although preliminary dilution of the suspensions to the nanosheet concentration of 15–20 mg/L did not allow us to completely prevent particle overlapping, one can observe, among other things, separate nanosheets. The main part of HBN<sub>3</sub> NSs has a relatively regular rectangular shape with lateral dimensions of 20–60 nm, which is somewhat smaller than reported in previous publications on the exfoliation of related niobates [11,13,17,21,40,41]. This difference may be caused by various reasons including unequal conditions of sonication and centrifugation. In particular, the relatively long time of the latter used in this study (1 h at a separation factor  $F = 1000$ ) could be the reason for the preservation of only fine nanosheet fractions in the resulting supernatant. Analysis of the HBN<sub>3</sub> NSs by means of HR-TEM and SAED (Figure S2) revealed the main interplanar distances in their structure including 3.82–3.86 Å for HCN<sub>3</sub> NSs and 3.86–3.90 Å for HSN<sub>3</sub> NSs, which are consistent with the  $a$  tetragonal lattice parameters determined from the XRD data (Table 1).

Particle sizes in the suspensions of pristine nanosheets were roughly estimated by the DLS method. The particle size distributions measured are predominantly monomodal with maxima at 86 and 47 nm for HCN<sub>3</sub> and HSN<sub>3</sub> NSs, respectively (Figure 4, Table 1). Unlike the distribution for HCN<sub>3</sub> NSs, that for HSN<sub>3</sub> ones is asymmetric with a wide shoulder in the region of large radii. The distribution for HCN<sub>3</sub> NSs also contains an additional maximum at 19 nm. Its assignment, unfortunately, has not been established exactly but it might refer to a finer nanosheet fraction. The hydrodynamic radii measured by DLS are seen to be greater than the lateral particle sizes determined by TEM. However, it is important to take into account that the processing of the DLS data was carried out assuming a spherical shape of the dispersed particles, which is very different from that of the nanosheets obtained. With this in mind, the size distributions presented may serve only as the estimation for the order of magnitude of the nanosheet size, which is consistent with the TEM data.

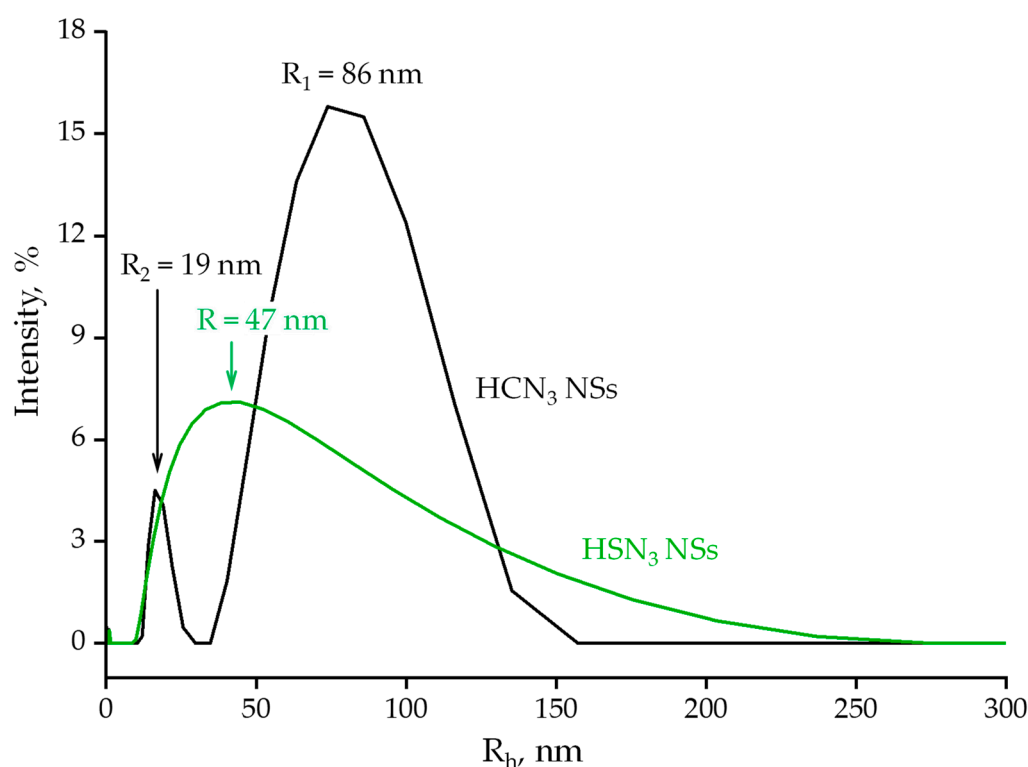


**Figure 4.** Particle size distributions in as-prepared suspensions of HBN<sub>3</sub> nanosheets.

Morphology of the powder samples was examined by SEM (Figure 5). The initial protonated niobates have monolithic plate-like particles with lateral dimensions of 500–1000 nm and a thickness of 150–300 nm and do not show any signs of the crystal delamination. Both types of the reassembled nanosheets, on the contrary, are seen to be relatively disordered aggregates of irregular quasi-lamellar particles separated by a large number of voids. However, HBN<sub>3</sub> HCl-restacked NSs are smaller in size, more distorted and form a more disordered aggregate in general than HBN<sub>3</sub> filtered NSs. Despite these morphological features, the specific surface area of HBN<sub>3</sub>-filtered NSs exceeds that of the protonated precursors by only two- to three-times (Table 1). At the same time, HCl-restacked NSs outperform the initial protonated niobates in the specific surface by up to 33 times, which may originate from their smaller particle sizes.

Of particular interest is the question of what relative sizes niobate particles have in the real photocatalytic suspensions. This issue may be considered indirectly based on the appearance of corresponding UV-vis spectra (Figure 6). A typical spectrum of the suspended protonated niobate exhibits nonzero and approximately constant optical density at all wavelengths without expressed maxima due to Mie scattering on relatively large particles. The pristine niobate nanosheets after exfoliation, on the contrary, give pronounced spectral bands only in the ultraviolet region ( $\lambda < 300$  nm) while optical density in the visible range tends to zero. Such appearance of UV-vis spectra is also typical of the nanosheets derived from other layered perovskite-like oxides [42]. The spectra of both types of reassembled nanosheets after redispersing allow one to assume that their particles are a cross between those of HBN<sub>3</sub> and HBN<sub>3</sub> NSs. Indeed, the spectra show clear maxima in the ultraviolet region whilst optical density in the visible range is nonzero. Despite that, HCl-restacked NSs clearly differ from filtered NSs by less pronounced ultraviolet bands and greater scattering of visible light. These experimental data indicate that the reassembled nanosheets (especially HCl-restacked ones) are not amenable to such redispersing that would have completely restored particle sizes and morphology typical of the pristine nanosheets after exfoliation. An additional interesting fact is that HBN<sub>3</sub> HCl-restacked NSs possess a four- to ten-times greater specific surface area in comparison with HBN<sub>3</sub> filtered NSs (Table 1) while the UV-vis spectrum appearance points to larger particle sizes of the

former sample. The key to this apparent contradiction, probably, is that the specific surface area is measured for a dry sample whereas the spectrum is recorded for a suspended one. If  $\text{HBN}_3$ -filtered NSs are redispersed easier than  $\text{HBN}_3$  HCl-restacked NSs due to greater destructibility of the aggregates during sonication, the former may give smaller particles in the final suspension and, thus, provide weaker light scattering in the visible spectrum region.

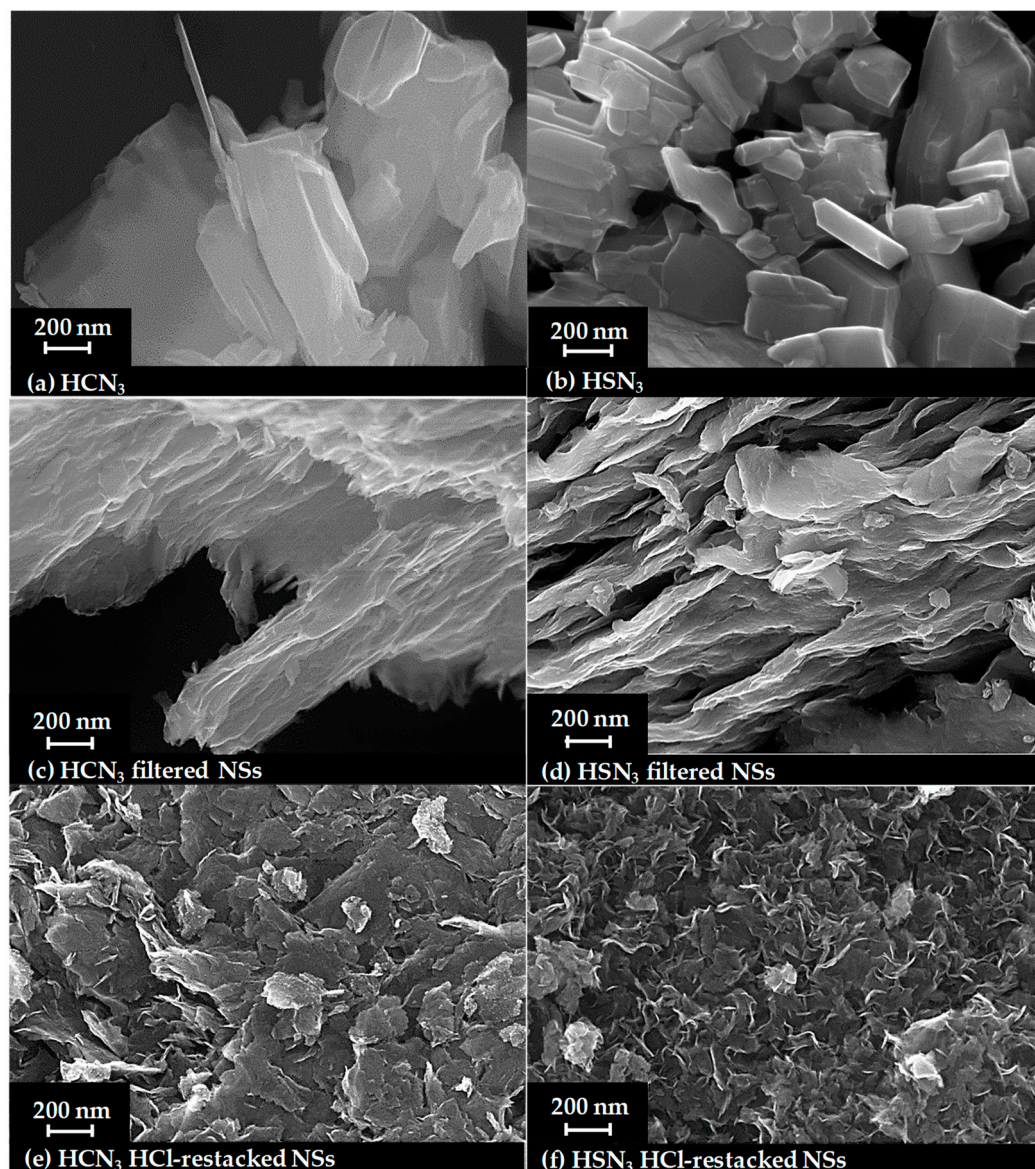


**Figure 5.** SEM images of the protonated niobates (a,b), their filtered (c,d) and HCl-restacked nanosheets (e,f).

The typical pH of the nanosheet suspensions obtained in 0.004 M TBAOH is 11.6–11.7. However, such a high pH value is unfavorable for the photocatalytic hydrogen generation [43]. In view of this, it is vital to determine the range within which pH can be varied to optimize the photocatalytic performance while avoiding strong particle agglomeration and subsequent sedimentation. The corresponding experiments and their results are described in details in Information S1. In brief, the suspensions of  $\text{HBN}_3$  NSs were found to be stable in the range of  $5 \leq \text{pH} \leq 11.75$ , which corresponds to  $\zeta$ -potential values  $-26.5 \leq \zeta \leq -23.0$  mV for  $\text{HCN}_3$  and  $-24.0 \leq \zeta \leq -20.0$  mV for  $\text{HSN}_3$ . When the pH becomes below 4 or above 12, the suspensions immediately flocculate.

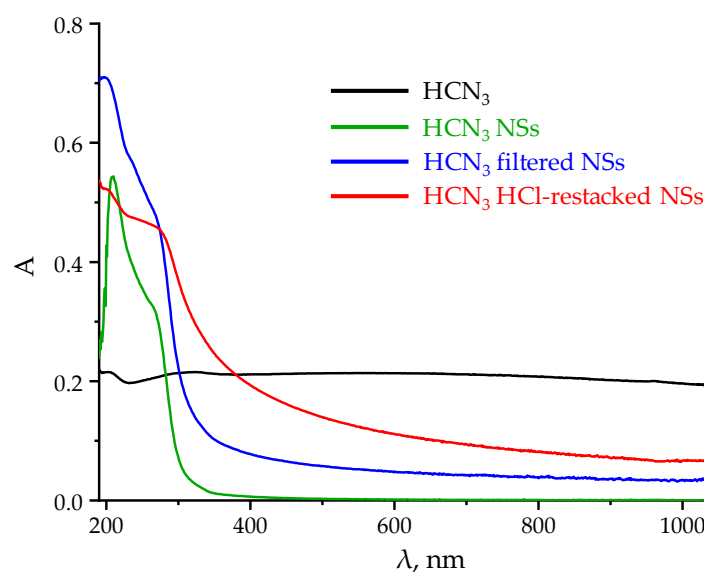


**Figure 6.** Typical UV-vis spectra of the suspensions of  $\text{HCN}_3$ , its pristine as well as reassembled and redispersed nanosheets.

## 2.2. Photocatalytic Activity with Respect to Hydrogen Production

The general mechanism of photocatalytic hydrogen evolution from water and aqueous solutions of organic substrates over suspended semiconductor particles may be described as follows [44–47]. The absorption of a photon with energy greater than the photocatalyst bandgap  $E_g$  leads to the formation of an electron-hole pair. When the electrons and holes are trapped at the surface of the photocatalyst, they may participate in redox reactions at the semiconductor-liquid interface. From thermodynamic point of view, the possibility of a given reduction or oxidation half-reaction is determined by the relation between the corresponding redox potential in solution and the quasi-Fermi levels for electrons and holes under irradiation, which can be roughly approximated by the conduction and valence band edges. The most common undesirable side process limiting the efficiency of photocatalysis is the electron-hole recombination. To minimize its negative impact, it is helpful to provide spatial separation of electrons and holes. Among several ways to achieve this, the most typical is the modification of the photocatalyst surface by an appropriate cocatalyst. Such a cocatalyst not only serves as a sink for electrons (or holes) but also catalyzes the corresponding reduction (or oxidation) reaction.

In case of the photocatalytic system under study, three main half-reactions should be considered. The first one is the reaction of hydrogen reduction, which in an acidic medium can be written as



This half-reaction accounts for the observed hydrogen production. It is efficiently promoted by the platinum cocatalyst nanoparticles deposited on the photocatalyst surface. The second half-reaction is associated with oxygen formation



The combination of half-reactions (1) and (2) corresponds to the overall water splitting. However, the half-reaction (2) is kinetically hindered and, therefore, occurs only in pure water, i.e., in the absence of other substrates, which may be oxidized easily. In the case of aqueous methanol solution, this half-reaction is readily substituted by the reaction of methanol oxidation



which is more favorable both from a thermodynamic and kinetic point of view. Depending on reaction conditions, the formaldehyde formed may be further oxidized to yield formic

acid or carbon dioxide. Thus, the overall photocatalytic reaction occurring in the presence of methanol is the dehydrogenation of the alcohol. Since the reduction and oxidation processes always proceed at equal rate, it is natural that the replacement of the unfavorable half-reaction of water oxidation typically leads to a significant increase in the hydrogen evolution rate.

In this study, the pristine niobate nanosheets and their reassembled forms have been thoroughly investigated as heterogeneous photocatalysts of hydrogen production from 1 mol.% aqueous methanol (Figures 7, S3 and S4) as well as pure distilled water (Figures S5–S7). The kinetic curves obtained demonstrate a predominantly linear course indicating the stable photocatalytic reaction rate throughout the measurement time. The exceptions are some platinized samples tested in pure water ( $\text{HCN}_3/\text{Pt}$ ,  $\text{HSN}_3/\text{Pt}$ ) whose curves show a so-called induction period during which the photocatalyst is being activated and the reaction rate is low (Figure S5). This activation effect, apparently, is caused by a time-consuming process of a Pt cocatalyst reduction. The latter is employed to suppress surface electron-hole recombination and create new active sites for hydrogen evolution due to which the platinized photocatalysts usually demonstrate much greater hydrogen evolution activity in comparison with bare ones [48]. All the photocatalytic experiments also included dark stages during which the reaction suspension was not irradiated. The corresponding sections of the hydrogen evolution curves reached a plateau indicating a zero reaction rate in the dark mode.

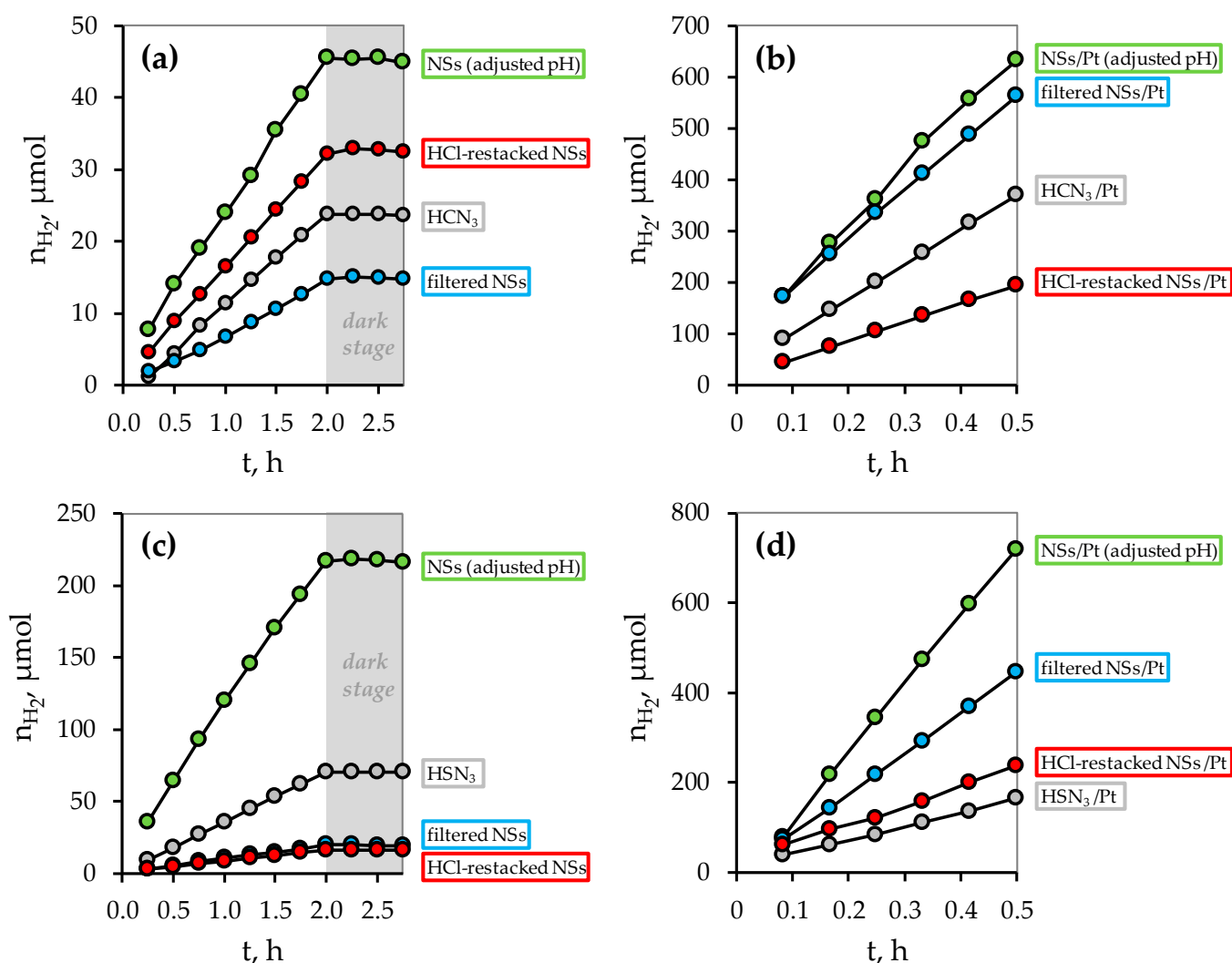


**Figure 7.** Kinetic curves of photocatalytic hydrogen evolution from 1 mol.% aqueous methanol over the  $\text{HCN}_3$  (a,b) and  $\text{HSN}_3$  (c,d) protonated niobates and their nanosheet-based photocatalysts.

Initial protonated niobates  $\text{HCN}_3$  and  $\text{HSN}_3$  were shown to provide apparent quantum efficiency  $\varphi$  of hydrogen generation from aqueous methanol of 0.17% and 0.48%, respectively. After the surface modification with a 1% Pt cocatalyst, the efficiency increased to 7.8% and 5.2% (Table 2)—relatively high values for the protonated perovskite-like oxides [47]. However,  $\text{HCN}_3$  NSs tested at the initial suspension pH  $\approx 11.6$  exhibited four- to five-times lower hydrogen evolution activity in comparison with the bulk precursors. This result was quite expected based on the literature data: excessively high pH leads to the dissociation of hydroxy groups on the photocatalyst surface, which adversely affects the photocatalytic performance [43]. Indeed, when pH was shifted to a subacidic range typical of the protonated niobates, the hydrogen generation rate increased drastically providing an impressive quantum efficiency of 20.1% and 20.8% over platinized  $\text{HCN}_3$  NSs and  $\text{HSN}_3$  NSs, respectively. Although the pH adjustment inevitably resulted in moderate lowering the suspension stability ( $c_2/c_1$  value decreased) (Table 2), it did not affect the stability of the hydrogen evolution rate.

Unlike the aforementioned  $\text{HBN}_3$  NSs, both filtered and HCl-restacked NSs did not outperform the protonated niobates in the photocatalytic activity being studied without a cocatalyst. This fact may potentially originate from the expressly disordered nature of the reassembled samples and absence of the chemically active interlayer space, which may be considered an additional reaction zone in the case of the bulk protonated niobates. However, this problem can be overcome by the platinization greatly improving surface charge separation. The quantum efficiency exhibited by the resulting platinized  $\text{HCN}_3$  filtered NSs and  $\text{HSN}_3$  filtered NSs reaches 20.4% and 12.2%, respectively. At the same time,  $\text{HBN}_3$  HCl-restacked NSs after platinization show only  $\varphi = 3.7\%$ , which is 1.5–2 times lower than the activity of the protonated precursors (Table 2). Moreover, the HCl-restacked NSs demonstrated the lowest stability towards sedimentation during photocatalytic measurements.

An investigation of the same photocatalysts in the water splitting reaction revealed in general the same trends as observed above (Table 2). Particularly, the hydrogen generation activity was found to be strongly pH-dependent: a pH shift from 11.7 to 4.9 allowed magnifying the reaction rate up to ten times. The greatest quantum efficiency of hydrogen evolution of 2.4% was observed over platinized  $\text{HCN}_3$  filtered NSs while the initial bulk niobate showed  $\varphi = 0.25\%$ . Among platinized  $\text{HSN}_3$ -based samples, the highest efficiency of 1.3% was exhibited by  $\text{HSN}_3$  NSs while the bulk precursor demonstrated only  $\varphi = 0.03\%$ . At the same time, the activity of  $\text{HBN}_3$  HCl-restacked NSs proved to be 2–3.5 times lower in comparison with that of the filtered analogues.

Long-term stability of the most active photocatalysts ( $\text{HBN}_3$  NSs/Pt and  $\text{HBN}_3$  filtered NSs/Pt) was evaluated via performing several running cycles in aqueous methanol with total duration of 12 h (Figure S8). It was shown that the hydrogen evolution activity not only does not decrease for six cycles but even slightly increases in the case of the  $\text{HBN}_3$  filtered NSs. XRD patterns of the nanosheet-based samples separated after photocatalytic experiments (Figure S9) exhibit the main diffraction peaks of the layered perovskite-like matrix confirming the structural stability of the photocatalysts under consideration. SEM images of the final samples (Figure S10) indicate the preservation of their morphology (the reassembled catalysts are still relatively disordered aggregates of quasi-lamellar particles) and also clearly show the presence of the Pt cocatalyst as light dots of 5–7 nm in size on the sample surface.

**Table 2.** Data on photocatalytic activity of protonated niobates and their nanosheets, pH (pH<sub>1</sub>—before, pH<sub>2</sub>—after photocatalytic experiment) and sedimentation stability of the reaction suspensions (c<sub>2</sub>/c<sub>1</sub>—ratio of volume photocatalyst concentrations at the ending and at the beginning of the photocatalytic experiment) as well as photon flux *f* in the photocatalysts' absorption range.

	Photocatalyst	$\omega$ , $\mu\text{mol/h}$	$\varphi$ , %	$k_{\text{Pt}}$	pH <sub>1</sub>	pH <sub>2</sub>	c <sub>2</sub> /c <sub>1</sub>	<i>f</i> , mmol/h	
1% (mol.) aq. CH <sub>3</sub> OH	HCN <sub>3</sub>	13	0.17	—	4.2	4.0	0.96	15.0	
	HCN <sub>3</sub> /Pt	590	7.8	45	3.5	3.2	0.97		
	HCN <sub>3</sub> NSs	initial pH	2.4	0.04	—	11.6	11.6	0.96	11.8
		adjusted pH	22	0.36	—	4.6	4.6	0.70	
	HCN <sub>3</sub> NSs/Pt	initial pH	82	1.4	34	11.5	11.4	0.96	
		adjusted pH	1190	20.1	54	4.0	3.6	0.86	
	HCN <sub>3</sub> filtered NSs	7.4	0.16	—	6.2	6.1	0.90	9.2	
	HCN <sub>3</sub> filtered NSs/Pt	940	20.4	127	5.1	4.2	0.59		
	HCN <sub>3</sub> HCl-restacked NSs	15	0.16	—	5.5	5.4	0.46	18.9	
	HCN <sub>3</sub> HCl-restacked NSs/Pt	350	3.7	23	4.6	4.3	0.43		
	HSN <sub>3</sub>	35	0.48	—	4.7	4.5	0.78	14.7	
	HSN <sub>3</sub> /Pt	380	5.2	11	4.6	4.1	0.68		
	HSN <sub>3</sub> NSs (adjusted pH)	100	1.4	—	5.7	5.7	0.89		
	HSN <sub>3</sub> NSs/Pt (adjusted pH)	1530	20.8	15	4.1	3.8	0.92		
	HSN <sub>3</sub> filtered NSs	9.5	0.13	—	7.0	7.0	0.98		
	HSN <sub>3</sub> filtered NSs/Pt	900	12.2	95	5.0	4.2	0.49		
	HSN <sub>3</sub> HCl-restacked NSs	7.8	0.08	—	5.8	4.9	0.47	19.4	
	HSN <sub>3</sub> HCl-restacked NSs/Pt	360	3.7	46	4.5	4.1	0.44		
	H <sub>2</sub> O	HCN <sub>3</sub>	4.0	0.09	—	4.5	4.5	0.49	9.2
		HCN <sub>3</sub> /Pt	11	0.25	3	4.2	4.3	0.85	
HCN <sub>3</sub> NSs		initial pH	1.2	0.02	—	11.7	11.7	0.97	11.8
		adjusted pH	12	0.2	—	4.9	4.9	0.12	
HCN <sub>3</sub> NSs/Pt		initial pH	40	0.69	33	11.6	11.4	0.92	
		adjusted pH	120	2.1	10	4.2	4.0	0.29	
HCN <sub>3</sub> filtered NSs		1.4	0.03	—	7.0	6.8	0.83	9.2	
HCN <sub>3</sub> filtered NSs/Pt		110	2.4	79	5.4	4.5	0.44		
HCN <sub>3</sub> HCl-restacked NSs		1.6	0.02	—	6.6	6.4	0.60	18.9	
HCN <sub>3</sub> HCl-restacked NSs/Pt		62	0.70	39	5.0	4.6	0.35		
HSN <sub>3</sub>		0.58	0.01	—	5.1	5.5	0.26	14.7	
HSN <sub>3</sub> /Pt		1.8	0.03	3	4.5	4.8	0.75		
HSN <sub>3</sub> NSs (adjusted pH)		4.7	0.06	—	5.6	5.6	0.28		
HSN <sub>3</sub> NSs/Pt (adjusted pH)		99	1.3	21	4.7	4.7	0.66		
HSN <sub>3</sub> filtered NSs		2.1	0.03	—	6.6	6.1	0.88		
HSN <sub>3</sub> filtered NSs/Pt		50	0.68	24	5.2	4.8	0.52		
HSN <sub>3</sub> HCl-restacked NSs	0.48	0.005	—	6.8	5.7	0.62	19.4		
HSN <sub>3</sub> HCl-restacked NSs/Pt	30	0.31	62	4.8	4.7	0.37			

Thus, exfoliation of the niobates into nanosheets allowed increasing the hydrogen evolution activity up to 55 times and reach quantum efficiency of 20.8% after surface

platinization. The maximum reaction rates in aqueous methanol reached over platinized  $\text{HCN}_3$  ( $47.6 \text{ mmol}\cdot\text{h}^{-1}\cdot\text{g}^{-1}$ ) and  $\text{HSN}_3$  nanosheets ( $61.2 \text{ mmol}\cdot\text{h}^{-1}\cdot\text{g}^{-1}$ ) exceed the literature values for the relative nanosheet-based samples [9] by approximately seven times. Nevertheless, no strict comparison is possible in this case since the literature does not provide quantum efficiency while the reaction conditions (namely, the irradiation used) are not completely identical. However, this is not the most interesting result. A much more intriguing factor is the significantly lower activity of the platinized  $\text{HBN}_3$  HCl-restacked NSs as compared to that of the simply filtered NSs (Figure 8) despite a four- to ten-times greater specific surface area of the former. Specific surface area is known to be one of the key parameters of any heterogeneous photocatalyst predetermining a number of active sites involved in the reaction. In view of this, an increase in the specific surface usually has a beneficial effect on photocatalytic performance [47]. Nevertheless, in this study the opposite is observed. As previously assumed, one of probable reasons for the greater photocatalytic activity of the  $\text{HBN}_3$  filtered NSs may consist in their better dispersibility in aqueous media during sonication. In other words, the aggregate of the filtered NSs might be less stable towards ultrasonic delamination in comparison with that of the HCl-restacked NSs. If this is indeed the case, the filtered NSs can give smaller particles in the final suspensions than the HCl-restacked ones and, thereby, surpass them in the active surface in the redispersed state. These assumptions are supported by the UV-vis spectra of the suspensions described above (Figure 6). Another possible reason may originate from different chemical compositions of two types of reassembled nanosheets. As shown above, the  $\text{HBN}_3$  HCl-restacked NSs are practically devoid of residual organics whilst the  $\text{HBN}_3$  filtered NSs contain a perceptible amount of tetrabutylammonium and, strictly speaking, represent hybrid inorganic-organic particles. As reported earlier, the organic modification of the interlayer space of layered perovskite-like oxides can greatly enhance the hydrogen evolution activity [29–31,49,50]. Although the filtered NSs with the tetrabutylammonium adsorbed and/or inserted into the voids between the reassembled particles are not completely similar to the mentioned inorganic-organic compounds, it appears reasonable to assume that the residual tetrabutylammonium can also have a beneficial effect on the photocatalytic activity. Particularly, it can hypothetically serve as a reducing agent promoting the Pt cocatalyst deposition or facilitate adsorption of the reactants in the course of photocatalysis. However, a separate study is required to clarify these assumptions.

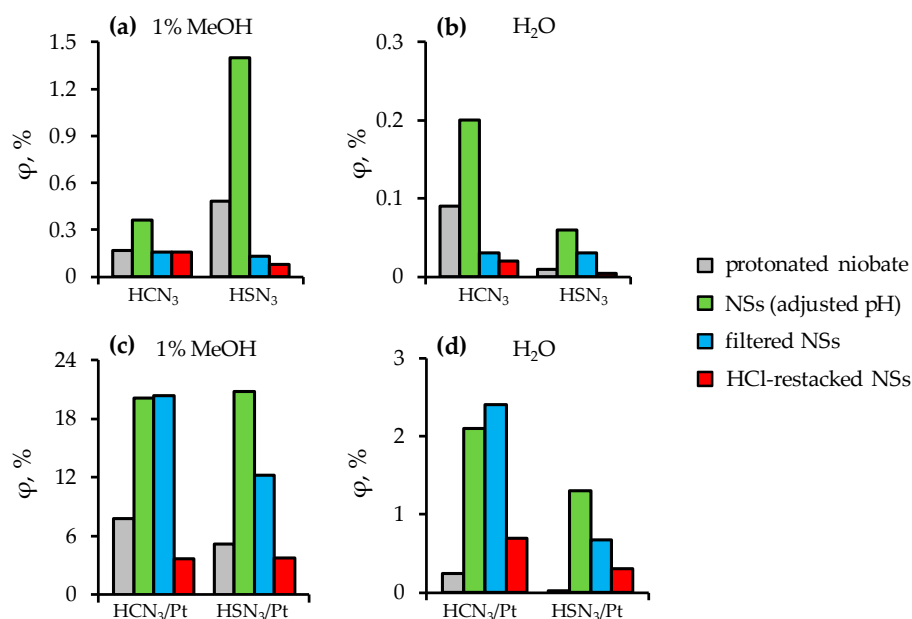


**Figure 8.** Comparison of apparent quantum efficiency of hydrogen generation from 1 mol.% aqueous methanol and water over the protonated niobates and their nanosheet-based photocatalysts in a bare state (a,b) and after surface platinization (c,d).

### 3. Materials and Methods

#### 3.1. Synthesis of Initial Protonated Niobates

Alkaline-layered perovskite-like niobates  $\text{KCa}_2\text{Nb}_3\text{O}_{10}$  ( $\text{KCN}_3$ ) and  $\text{KSr}_2\text{Nb}_3\text{O}_{10}$  ( $\text{KSN}_3$ ) were synthesized in accordance with the conventional ceramic method using pre-calcined  $\text{Nb}_2\text{O}_5$ ,  $\text{CaO}$  (or  $\text{SrCO}_3$ ) and  $\text{K}_2\text{CO}_3$  as reactants (Vekton, Saint Petersburg, Russia). The oxides and strontium carbonate were taken in stoichiometric amounts, potassium carbonate was weighed with a 30% excess to compensate for the loss during calcination. The reactants were mixed in a grinding bowl with silicon nitride balls and ground under an *n*-heptane layer in a Fritsch Pulverisette 7 planetary micro mill (Idar-Oberstein, Germany) at a rotation speed of 600 rpm, using a program of 10 repetitions of 10 min each separated by 5 min intervals. The mixture obtained was dried and pelletized into ~2 g tablets at a pressure of 50 bar using an Omec PI 88.00 hydraulic press (Certaldo, Italy). Then, the tablets were placed into corundum crucibles with lids, calcined in a Nabertherm L-011K2RN muffle furnace (Lilienthal, Germany) and, after cooling down, ground in an agate mortar. The temperature program of  $\text{KCN}_3$  synthesis consisted of two stages (800 °C for 12 h and 1100 °C for 24 h) with intermediate grinding and re-pelletizing.  $\text{KSN}_3$  was prepared via one-stage calcination (1300 °C for 10 h).

To obtain protonated hydrated niobates  $\text{HCN}_3$  and  $\text{HSN}_3$ , the powders of  $\text{KCN}_3$  and  $\text{KSN}_3$  were treated with a 100-fold molar excess of 12 M nitric acid (Vekton, Saint Petersburg, Russia) for 1 d and 6 M nitric acid for 2 d, respectively. After this, the products were centrifuged, thoroughly rinsed with water to remove acid residues and dried under ambient pressure. To avoid dehydration, the  $\text{HBN}_3$  samples were further stored in an atmosphere of humid air.

#### 3.2. Exfoliation into Nanosheets and Their Reassembly

To prepare the suspension of the niobate nanosheets ( $\text{HBN}_3$  NSs), a weight of the protonated hydrated niobate (54 mg of  $\text{HCN}_3$  or 64 mg of  $\text{HSN}_3$ ) was placed into a tube with 50 mL of 0.004 M aqueous TBAOH (Acros Organics, New Jersey, USA) and sonicated by a Hielscher UP200St (200 W) homogenizer (Teltow, Germany) at half power for 5 min. After shaking at room temperature for 7 d, the mixture was sonicated for 5 min again. Hereafter bulk non-exfoliated particles were sedimented on a laboratory centrifuge ELMi CM-6MT (Riga, Latvia) at a separation factor  $F = 1000$  for 1 h and the target suspension of the nanosheets was carefully separated from the precipitate with a pipette. The weights of the precursors and TBAOH concentration were calculated in such a way as to provide a ratio of  $\text{TBA}^+$  cations to interlayer vertices of perovskite octahedra equal to 1:1. The exfoliation experiments were repeated several times to obtain the required suspension volumes.

$\text{HBN}_3$  filtered NSs were obtained via the vacuum filtration of the aforementioned suspensions on membrane Teflon filters with a pore size of 200 nm at a rate of 50 mL of the suspension per one filter. The samples were rinsed with an excess of hot water, dried under ambient conditions and removed from the filters with a spatula.

To obtain  $\text{HBN}_3$  HCl-restacked NSs, the aforementioned suspensions of the exfoliated niobates were acidified by 1 M hydrochloric acid under continuous stirring to cause the formation of a flocculent precipitate ( $\text{pH} < 4$ ), which was then filtered, rinsed and collected as described above. A generalized scheme for obtaining differently reassembled nanosheets is shown in Figure 9.

#### 3.3. Investigation of Nanosheet Suspension Stability in Relation to pH Shifts

Stability of the suspensions with respect to fast flocculation of the nanosheets at various pH was studied via the visual control of the homogeneity of the red laser beam being scattered by the dispersed particles (a Tyndall effect). During the experiment, the suspension was intensely stirred by a magnetic stirrer and pH was changed by the dropwise addition of 0.01 M hydrochloric acid or potassium hydroxide. The experiment was finished at such a pH value when a flocculent precipitate was immediately formed. Hereafter, a series of nanosheet suspensions with pH values falling into the stability range was

analyzed to measure a  $\zeta$ -potential. The results obtained were presented as a dependence of the  $\zeta$ -potential on pH of the medium.

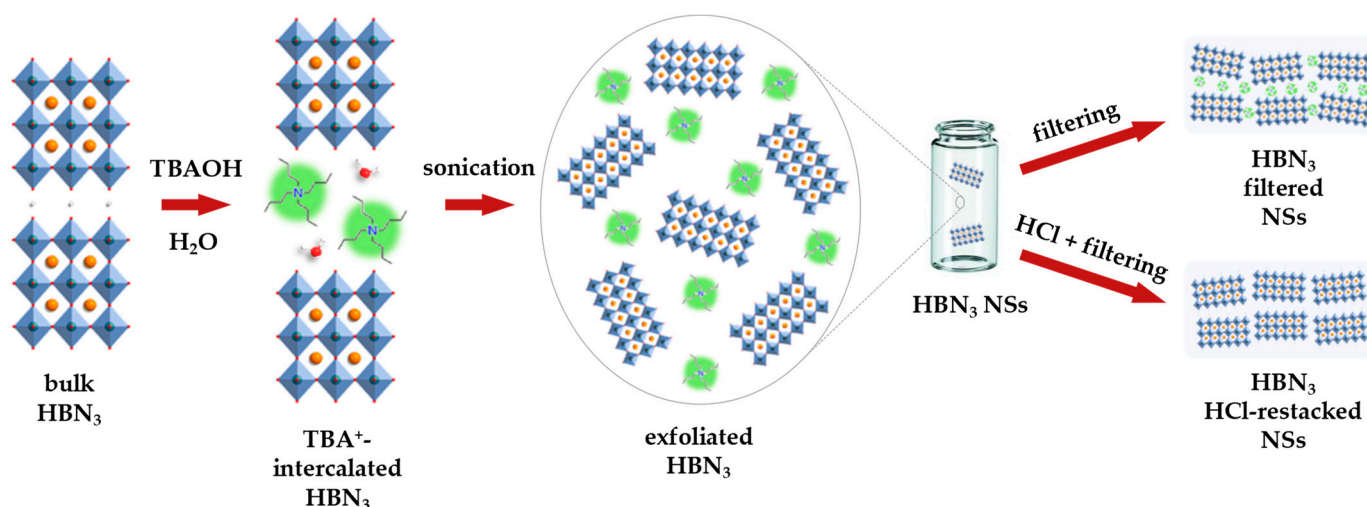


**Figure 9.** Exfoliation of the protonated niobates into nanosheets and two approaches to their reassembly.

### 3.4. Investigation of Photocatalytic Activity in the Reactions of Hydrogen Production

Photocatalytic activity was studied in relation to light-driven hydrogen production from 1 mol.% aqueous methanol as well as pure water under near-ultraviolet irradiation. The main aim was to compare the activity of three types of exfoliated niobates—pristine, filtered and HCl-restacked nanosheets. All the samples were tested both in a bare state and after surface modification with a 1% Pt cocatalyst. The measurements were performed on the laboratory photocatalytic setting used in our previous reports [29–31,49–51] and included determination of the hydrogen generation rate  $\omega$ , apparent quantum efficiency  $\varphi$  and multiplicity of the increase in the rate after Pt loading (platinization increase factor  $k_{Pt}$ ) as quantitative indicators of the photocatalytic performance. The detailed description of the experimental setting used and method for quantum efficiency calculation are presented in Informations S2 and S3. Emission spectrum of the lamp is shown in Figure S11.

Detailed procedures for the investigation of the photocatalytic activity are described in Information S4. Briefly, powder samples (protonated niobates and reassembled nanosheets) were dispersed in aqueous methanol or distilled water, loaded into the reaction cell and purged with argon to remove residual air. When studying the activity with the Pt cocatalyst, a H<sub>2</sub>PtCl<sub>6</sub> aqueous solution was injected into the suspension to perform in situ photocatalytic platinization. The reaction suspension, being continuously stirred, was irradiated by a 125 W mercury lamp through a cut-off filter (transmittance  $\lambda > 220$  nm) and the hydrogen content in the gas circuit was analyzed chromatographically at regular time intervals. The reaction suspension volume, photocatalyst concentration and Pt content in the sample were 50 mL, 500 mg/L and 1%, respectively. The duration of a kinetic curve accumulation was 2 h, which was followed by a dark stage monitoring potential activity of the sample without irradiation. Before testing the activity of pristine nanosheets without reassembly, their TBAOH-containing suspensions were diluted to 500 mg/L. When required, hydrochloric acid, methanol and H<sub>2</sub>PtCl<sub>6</sub> were added to provide the same pH, sacrificial agent concentration and cocatalyst content as in the experiments with the powder samples. Other experimental conditions and procedures were the same. Long-term stability of the most active photocatalysts was evaluated in the reaction of hydrogen production from aqueous methanol via performing several running cycles with a total duration of 12 h.

At the beginning and ending of the photocatalytic experiment, a pH value and a UV-vis spectrum of the reaction suspension were measured. The stability of each suspension towards sedimentation was evaluated by the  $c_2/c_1$  ratio, where  $c_2$  and  $c_1$  are volume

photocatalyst concentrations at the ending and at the beginning of the photocatalytic experiment, respectively. This ratio stands for the fraction of the photocatalyst remained in the volume of the suspension by the end of the experiment while the expression  $1 - c_2/c_1$  gives the fraction of the sedimented sample. The  $c_2/c_1$  ratio was assumed to be equal to the ratio of optical densities  $A_2/A_1$  from the UV-vis spectrum at equal dilutions of the suspensions ( $\lambda = 550$  nm for both HBN<sub>3</sub> protonated niobates,  $\lambda = 230$  nm for all the HCN<sub>3</sub> nanosheet-based samples,  $\lambda = 255$  nm for all the HSN<sub>3</sub> nanosheet-based ones).

### 3.5. Instrumentation

#### 3.5.1. XRD

Powder X-ray diffraction (XRD) analysis of the samples was performed on a Rigaku Miniflex II benchtop diffractometer (Tokyo, Japan) using CuK $\alpha$  radiation, an angle range  $2\theta = 3\text{--}60^\circ$  and a scanning rate of  $10^\circ/\text{min}$ . In the case of reassembled samples, the tetragonal lattice parameters were approximately calculated after taking into account the X-ray diffractometer zero shift based on the position of the most intense reflections with indices (001), (010), (110) and (020) (Figure 1).

#### 3.5.2. Raman Spectroscopy

Raman scattering spectra were collected on a Bruker Senterra spectrometer (Billerica, MA, USA) in the Raman shift range of  $50\text{--}4000$  cm<sup>-1</sup> using a 532 nm laser (power 5 mW, accumulation time 30 s, 4 repetitions).

#### 3.5.3. TG

Thermogravimetric (TG) analysis was performed on a Netzsch TG 209 F1 Libra thermobalance (Selb, Germany) in a synthetic air atmosphere (temperature range  $30\text{--}950$  °C, heating rate  $10$  °C/min).

#### 3.5.4. CHN-Analysis

The carbon, hydrogen and nitrogen content in the reassembled nanosheets was determined via the elemental CHN-analysis on a Euro EA3028-HT analyzer (Pavia, Italy).

#### 3.5.5. DRS

Diffuse reflectance spectra (DRS) were obtained on a Shimadzu UV-2550 spectrophotometer (Kyoto, Japan) with an ISR-2200 integrating sphere attachment in the range of  $220\text{--}800$  nm using barium sulphate as an external reference with reflection coefficient  $R = 1$ . The reflectance spectra were transformed into coordinates  $(F \cdot hv)^{1/2} = f(hv)$ , where  $F = (1 - R)^2 / 2R$  is the Kubelka-Munk function. Linear sections of the graph were extrapolated and an optical bandgap energy  $E_g$  was found as an abscissa of their intersection point.

#### 3.5.6. TEM

Morphology of the nanosheets was studied on a Zeiss Libra 200FE transmission electron microscope (TEM) (Oberkochen, Germany). The main interplanar distances were calculated based on high resolution TEM (HR-TEM) and selected area electron diffraction (SAED) data. Before the deposition on the sample holder, the TBAOH-containing suspensions of the exfoliated niobates were diluted with methanol to achieve the nanosheet concentration of  $\approx 15\text{--}20$  mg/L.

#### 3.5.7. SEM

Morphology of the bulk protonated niobates and reassembled nanosheets was investigated on a Zeiss Merlin scanning electron microscope (SEM) (Oberkochen, Germany) equipped with a field emission cathode, electron optics column Gemini II and oil-free vacuum system.

### 3.5.8. BET

Specific surface area of the powder samples was measured on a Quadrasorb SI (Boynton Beach, FL, USA) adsorption analyzer. Prior to analysis, 150–200 mg of each sample was degassed for 12 h without heating. Adsorption isotherms were measured at a liquid nitrogen temperature ( $-196\text{ }^{\circ}\text{C}$ ) with nitrogen as an adsorptive. The values of specific surface area were calculated via the conventional multipoint Brunauer-Emmett-Teller method (BET).

### 3.5.9. DLS

Particle size distributions and  $\zeta$ -potentials in the suspensions of nanosheets were estimated by the method of dynamic light scattering (DLS) on a Photocor Compact-Z analyzer (Moscow, Russia). The scattered light was detected at an angle of  $90^{\circ}$  and  $20^{\circ}$ , respectively.

### 3.5.10. ICP-AES

Concentrations of the niobate nanosheets in the suspensions, used for further building spectrophotometric calibration plots, were determined by inductively coupled plasma atomic emission spectroscopy (ICP-AES) on a Shimadzu ICPE-9000 spectrometer (Kyoto, Japan) after preliminary acid digestion.

### 3.5.11. UV-vis Spectrophotometry

Spectrophotometric analysis of the suspensions, used to control their stability and nanosheet concentration, was carried out on a Thermo Scientific Genesys 10S UV-Vis spectrophotometer (Waltham, MA, USA). Measurements were conducted in the range of optical density  $A < 2$ . The 1 mol.% aqueous methanol or pure distilled water were used for dilution and baseline recording. The spectrophotometric calibration plots for the express determination of nanosheet concentrations in the suspensions are presented in Information S5.

### 3.5.12. pH Measurement

The pH values of the reaction suspensions were controlled using a laboratory pH-meter Mettler Toledo SevenCompact S220 (Greifensee, Switzerland) equipped with an InLab Expert Pro-ISM electrode.

## 4. Conclusions

The present study has demonstrated that the photocatalytic activity of exfoliated layered perovskite-like niobates  $\text{HB}_2\text{Nb}_3\text{O}_{10}$  ( $B = \text{Ca}, \text{Sr}$ ) is strongly dependent on the form in which the resulting nanosheets are tested. In particular, the use of the pristine nanosheets without reassembly allows one to avoid their strong agglomeration and, thus, preserve a high active surface area, which results in high quantum efficiency of hydrogen evolution exceeding 20%. Among the reassembled samples modified with a Pt cocatalyst, significantly higher photocatalytic performance is exhibited by simply filtered nanosheets that, unlike the HCl-restacked ones, possess a much lower specific surface area in a dry state but contain a perceptible amount of residual tetrabutylammonium. At the same time, the nanosheet precipitation by acids, widely used in literature, appears not to be an optimal approach to the preparation of highly efficient nanosheet-based photocatalysts. The activity difference, potentially, is associated with the fact that the filtered nanosheets undergo ultrasonic disaggregation before photocatalytic tests much easier than their HCl-restacked counterparts and, thanks to this, possess greater active surface in the reaction suspension. In addition, the enhanced activity of the filtered nanosheets may be due to the presence of tetrabutylammonium as an organic modifier on their surface, which is consistent with high photocatalytic performance of organically modified layered perovskites considered in our previous reports. The novelty and practical importance of the present study consists in the examination of effective approaches to the preparation of reaction suspensions of well-known nanosheet-based photocatalysts, which, despite their simplicity, are practically

not covered in the available literature. These approaches lead to significantly greater performance of the photocatalytic suspensions obtained in comparison with the conventional acid precipitation and redispersing of the nanosheets, which opens up new possibilities for creating more efficient photocatalysts based on already reported layered materials.

**Supplementary Materials:** The following data are available online at <https://www.mdpi.com/article/10.3390/catal13030614/s1>, Figure S1: TG curves of the protonated forms and reassembled nanosheets of  $\text{HCN}_3$  and  $\text{HSN}_3$  niobates, Figure S2: Images of the niobate nanosheets obtained by TEM, HR-TEM and SAED patterns with main interplanar distances, Figure S3: Kinetic curves of photocatalytic hydrogen evolution from 1 mol.% aqueous methanol in the presence of 0.004 M TBAOH over pristine and Pt-loaded  $\text{HCN}_3$  nanosheets without medium acidification, Figure S4: Full kinetic curves of photocatalytic hydrogen evolution from 1 mol.% aqueous methanol over Pt-loaded  $\text{HBN}_3$  nanosheets, Figure S5: Kinetic curves of photocatalytic hydrogen evolution from water over initial and Pt-loaded protonated niobates  $\text{HBN}_3$ , Figure S6: Kinetic curves of photocatalytic hydrogen evolution from water over  $\text{HCN}_3$  nanosheet-based photocatalysts, Figure S7: Kinetic curves of photocatalytic hydrogen evolution from water over  $\text{HSN}_3$  nanosheet-based photocatalysts, Figure S8: Hydrogen generation rate from 1 mol.% aqueous methanol over Pt-loaded  $\text{HBN}_3$  nanosheet-based photocatalysts after several running cycles, Figure S9: XRD patterns of the reassembled nanosheets before and after photocatalysis (PC), Figure S10: SEM images of the reassembled nanosheets before and after photocatalysis (PC), Figure S11: Emission spectrum of the DRT-125 mercury lamp compared with the absorption regions of the photocatalysts under study, Information S1: Stability of the as-prepared nanosheet suspensions relative to fast flocculation upon pH shifts, Information S2: Scheme and operation principle of the photocatalytic setting, Information S3: Method for the calculation of apparent quantum efficiency, Information S4: Detailed procedure for the investigation of photocatalytic activity, Information S5: Spectrophotometric calibration plots for express measurement of nanosheet concentrations in suspensions.

**Author Contributions:** Conceptualization, O.I.S. and I.A.Z.; methodology, S.A.K., O.I.S. and V.V.V.; investigation, S.A.K., V.V.V. and E.N.M.; data curation, O.I.S. and I.A.R.; writing—original draft preparation, S.A.K. and O.I.S.; writing—review and editing, S.A.K., O.I.S. and I.A.R.; visualization, S.A.K. and I.A.R.; supervision, O.I.S. and I.A.Z.; funding acquisition, O.I.S.; project administration, I.A.Z. All authors have read and agreed to the published version of the manuscript.

**Funding:** The study was financially supported by Russian Science Foundation (project № 22-73-10110).

**Data Availability Statement:** The data presented in this study are available in the article.

**Acknowledgments:** The study was conducted using the equipment of the Saint Petersburg State University Research Park: Centre for X-ray Diffraction Studies, Centre for Optical and Laser Research, Centre for Chemical Analysis and Materials Research, Centre for Thermal Analysis and Calorimetry, Interdisciplinary Centre for Nanotechnology, Centre for Diagnostics of Functional Materials for Medicine, Pharmacology and Nanoelectronics. This article is dedicated to the 300th anniversary of Saint Petersburg State University.

**Conflicts of Interest:** The authors declare no conflict of interest.

## References

1. Schaak, R.E.; Mallouk, T.E. Perovskites by Design: A Toolbox of Solid-State Reactions. *Chem. Mater.* **2002**, *14*, 1455–1471. [[CrossRef](#)]
2. Uppuluri, R.; Sen Gupta, A.; Rosas, A.S.; Mallouk, T.E. Soft Chemistry of Ion-Exchangeable Layered Metal Oxides. *Chem. Soc. Rev.* **2018**, *47*, 2401–2430. [[CrossRef](#)] [[PubMed](#)]
3. Tani, S.; Komori, Y.; Hayashi, S.; Sugahara, Y. Local Environments and Dynamics of Hydrogen Atoms in Protonated Forms of Ion-Exchangeable Layered Perovskites Estimated by Solid-State  $1\text{H}$  NMR. *J. Solid State Chem.* **2006**, *179*, 3357–3364. [[CrossRef](#)]
4. Maeda, K.; Mallouk, T.E. Two-Dimensional Metal Oxide Nanosheets as Building Blocks for Artificial Photosynthetic Assemblies. *Bull. Chem. Soc. Jpn.* **2019**, *92*, 38–54. [[CrossRef](#)]
5. Lee, W.-J.; Yeo, H.J.; Kim, D.-Y.; Paek, S.-M.; Kim, Y.-I. Exfoliation of Dion-Jacobson Layered Perovskite into Macromolecular Nanoplatelet. *Bull. Korean Chem. Soc.* **2013**, *34*, 2041–2043. [[CrossRef](#)]
6. Jacobson, A.J.; Lewandowski, J.T.; Johnson, J.W. Ion Exchange of the Layered Perovskite  $\text{KCa}_2\text{Nb}_3\text{O}_{10}$  by Protons. *J. Less Common Met.* **1986**, *116*, 137–146. [[CrossRef](#)]

7. Jacobson, A.J.; Johnson, J.W.; Lewandowski, J.T. Interlayer Chemistry between Thick Transition-Metal Oxide Layers: Synthesis and Intercalation Reactions of  $K[Ca_2Na_{n-3}Nb_nO_{3n+1}]$  ( $3 \leq n \leq 7$ ). *Inorg. Chem.* **1985**, *24*, 3727–3729. [[CrossRef](#)]
8. Schaak, R.E.; Mallouk, T.E. Prying Apart Ruddlesden-Popper Phases: Exfoliation into Sheets and Nanotubes for Assembly of Perovskite Thin Films. *Solid State Ion.* **2000**, *12*, 3427–3434. [[CrossRef](#)]
9. Ebina, Y.; Sasaki, T.; Harada, M.; Watanabe, M. Restacked Perovskite Nanosheets and Their Pt-Loaded Materials as Photocatalysts. *Chem. Mater.* **2002**, *1*, 4390–4395. [[CrossRef](#)]
10. Maeda, K.; Mallouk, T.E. Comparison of Two- and Three-Layer Restacked Dion–Jacobson Phase Niobate Nanosheets as Catalysts for Photochemical Hydrogen Evolution. *J. Mater. Chem.* **2009**, *19*, 4813–4818. [[CrossRef](#)]
11. Zhou, H.; Sabio, E.M.; Townsend, T.K.; Fan, T.; Zhang, D.; Osterloh, F.E. Assembly of Core-Shell Structures for Photocatalytic Hydrogen Evolution from Aqueous Methanol. *Chem. Mater.* **2010**, *22*, 3362–3368. [[CrossRef](#)]
12. Yang, Y.; Xiong, J.; Song, Y.; Zou, J.; Wu, L. Preparation of Monolayer H<sub>Sr</sub> 2 Nb 3 O 10 Nanosheets for Photocatalytic Hydrogen Evolution. *Dalt. Trans.* **2019**, *48*, 11136–11141. [[CrossRef](#)] [[PubMed](#)]
13. Jiang, D.; Wang, T.; Xu, Q.; Li, D.; Meng, S.; Chen, M. Perovskite Oxide Ultrathin Nanosheets/g-C<sub>3</sub>N<sub>4</sub> 2D-2D Heterojunction Photocatalysts with Significantly Enhanced Photocatalytic Activity towards the Photodegradation of Tetracycline. *Appl. Catal. B Environ.* **2017**, *201*, 617–628. [[CrossRef](#)]
14. Xiong, J.; Jing, K.; Zou, J.; Liang, S.; Wu, L. A Hybrid of CdS/HCa<sub>2</sub>Nb<sub>3</sub>O<sub>10</sub> Ultrathin Nanosheets for Promoting Photocatalytic Hydrogen Evolution. *Dalt. Trans.* **2017**, *46*, 13935–13942. [[CrossRef](#)] [[PubMed](#)]
15. Ma, X.; Jiang, D.; Xiao, P.; Jin, Y.; Meng, S.; Chen, M. 2D/2D Heterojunctions of WO<sub>3</sub> Nanosheet/K+Ca<sub>2</sub>Nb<sub>3</sub>O<sub>10</sub><sup>−</sup> Ultrathin Nanosheet with Improved Charge Separation Efficiency for Significantly Boosting Photocatalysis. *Catal. Sci. Technol.* **2017**, *7*, 3481–3491. [[CrossRef](#)]
16. Sun, Y.; Wen, B.; Jiang, D.; Li, D. CdS Nanoparticles Decorated K<sup>+</sup>Ca<sub>2</sub>Nb<sub>3</sub>O<sub>10</sub><sup>−</sup> Nanosheets with Enhanced Photocatalytic Activity. *Mater. Lett.* **2018**, *229*, 236–239. [[CrossRef](#)]
17. Hu, Y.; Li, G.; Zong, S.; Shi, J.; Guo, L. Self-Assembled Nanohybrid of Cadmium Sulfide and Calcium Niobate: Photocatalyst with Enhanced Charge Separation for Efficient Visible Light Induced Hydrogen Generation. *Catal. Today* **2018**, *315*, 117–125. [[CrossRef](#)]
18. Liu, Y.; Zhou, Y.; Lv, C.; Zhang, C.; Jin, X.; Meng, Q.; Chen, G. Construction of 2D-Composite HCa<sub>2</sub>Nb<sub>3</sub>O<sub>10</sub>/CaNb<sub>2</sub>O<sub>6</sub> Heterostructured Photocatalysts with Enhanced Hydrogen Production Performance. *New J. Chem.* **2018**, *42*, 681–687. [[CrossRef](#)]
19. Li, D.; Zhao, H.; Li, L.; Mao, B.; Chen, M.; Shen, H.; Shi, W.; Jiang, D.; Lei, Y. Graphene-Sensitized Perovskite Oxide Monolayer Nanosheets for Efficient Photocatalytic Reaction. *Adv. Funct. Mater.* **2018**, *28*, 1806284. [[CrossRef](#)]
20. Luo, D.; Huang, Y.; Zhao, Y.; Fang, Y.; Li, Z.; Guo, Q.; Wei, Y.; Fan, L.; Wu, J. Visible-Light-Driven H<sub>Sr</sub>2Nb<sub>3</sub>O<sub>10</sub>/CdS Heterojunctions for High Hydrogen Evolution Activity. *Int. J. Hydrogen Energy* **2020**, *45*, 2896–2908. [[CrossRef](#)]
21. Ding, Y.; Luo, D.; Huang, Y.; Rong, B.; Chen, X.; Wei, Y.; Fan, L.; Wu, J. Microwave-Mechanochemistry-Assisted Synthesis of Z-Scheme H<sub>Sr</sub>2Nb<sub>3</sub>O<sub>10</sub>/WO<sub>3</sub> heterojunctions for Improved Simulated Sunlight Driven Photocatalytic Activity. *J. Environ. Chem. Eng.* **2021**, *9*, 104624. [[CrossRef](#)]
22. Dion, M.; Ganne, M.; Tournoux, M. Nouvelles Familles de Phases M<sup>I</sup>M<sup>II</sup><sub>2</sub>Nb<sub>3</sub>O<sub>10</sub> a Feuilletés “Perovskites”. *Mater. Res. Bull.* **1981**, *16*, 1429–1435. [[CrossRef](#)]
23. Fukuoka, H.; Isami, T.; Yamanaka, S. Crystal Structure of a Layered Perovskite Niobate KCa<sub>2</sub>Nb<sub>3</sub>O<sub>10</sub>. *J. Solid State Chem.* **2000**, *151*, 40–45. [[CrossRef](#)]
24. Jacobson, A.J.; Johnson, J.W.; Lewandowski, J. Intercalation of the Layered Solid Acid HCa<sub>2</sub>Nb<sub>3</sub>O<sub>10</sub> by Organic Amines. *Mater. Res. Bull.* **1987**, *22*, 45–51. [[CrossRef](#)]
25. Tahara, S.; Sugahara, Y. Interlayer Surface Modification of the Protonated Triple-Layered Perovskite HCa<sub>2</sub>Nb<sub>3</sub>O<sub>10</sub>·xH<sub>2</sub>O with n-Alcohols. *Langmuir* **2003**, *19*, 9473–9478. [[CrossRef](#)]
26. Domen, K.; Yoshimura, J.; Sekine, T.; Kondo, J.; Tanaka, A.; Maruya, K.; Onishi, T. A Novel Series of Photocatalysts with an Ion-Exchangeable Layered Structure of Niobate. In *Studies in Surface Science and Catalysis*; Elsevier: Amsterdam, The Netherlands, 1993; pp. 2159–2162.
27. Oshima, T.; Ishitani, O.; Maeda, K. Non-Sacrificial Water Photo-Oxidation Activity of Lamellar Calcium Niobate Induced by Exfoliation. *Adv. Mater. Interfaces* **2014**, *1*, 2–5. [[CrossRef](#)]
28. Sabio, E.M.; Chamousis, R.L.; Browning, N.D.; Osterloh, F.E. Photocatalytic Water Splitting with Suspended Calcium Niobium Oxides: Why Nanoscale Is Better than Bulk—A Kinetic Analysis. *J. Phys. Chem. C* **2012**, *116*, 3161–3170. [[CrossRef](#)]
29. Voytovich, V.V.; Kurnosenko, S.A.; Silyukov, O.I.; Rodionov, I.A.; Minich, I.A.; Zvereva, I.A. Study of N-Alkylamine Intercalated Layered Perovskite-Like Niobates HCa<sub>2</sub>Nb<sub>3</sub>O<sub>10</sub> as Photocatalysts for Hydrogen Production From an Aqueous Solution of Methanol. *Front. Chem.* **2020**, *8*, 300. [[CrossRef](#)] [[PubMed](#)]
30. Voytovich, V.V.; Kurnosenko, S.A.; Silyukov, O.I.; Rodionov, I.A.; Bugrov, A.N.; Minich, I.A.; Malygina, E.N.; Zvereva, I.A. Synthesis of N-Alkoxy Derivatives of Layered Perovskite-Like Niobate HCa<sub>2</sub>Nb<sub>3</sub>O<sub>10</sub> and Study of Their Photocatalytic Activity for Hydrogen Production from an Aqueous Solution of Methanol. *Catalysts* **2021**, *11*, 897. [[CrossRef](#)]
31. Kurnosenko, S.A.; Voytovich, V.V.; Silyukov, O.I.; Rodionov, I.A.; Zvereva, I.A. Photocatalytic Hydrogen Production from Aqueous Solutions of Glucose and Xylose over Layered Perovskite-like Oxides HCa<sub>2</sub>Nb<sub>3</sub>O<sub>10</sub>, H<sub>2</sub>La<sub>2</sub>Ti<sub>3</sub>O<sub>10</sub> and Their Inorganic-Organic Derivatives. *Nanomaterials* **2022**, *12*, 2717. [[CrossRef](#)]

32. Shi, J.; Mao, L.; Cai, C.; Li, G.; Cheng, C.; Zheng, B.; Hu, Y.; Huang, Z.; Hu, X.; Żyła, G. One-Pot Fabrication of 2D/2D  $\text{HCa}_2\text{Nb}_3\text{O}_{10}/\text{g-C}_3\text{N}_4$  type II Heterojunctions towards Enhanced Photocatalytic  $\text{H}_2$  evolution under Visible-Light Irradiation. *Catal. Sci. Technol.* **2020**, *10*, 5896–5902. [[CrossRef](#)]
33. Li, D.; Zhou, C.; Liang, X.; Shi, X.; Song, Q.; Chen, M.; Jiang, D. Noble-Metal-Free  $\text{Mo}_2\text{C}$  Co-Catalyst Modified Perovskite Oxide Nanosheet Photocatalysts with Enhanced Hydrogen Evolution Performance. *Colloids Surf. A Physicochem. Eng. Asp.* **2021**, *615*, 126252. [[CrossRef](#)]
34. Xie, Z.; Liang, X.; Jiang, D.; Chen, M. Noble-Metal-Free CoxP Nanoparticles: Modified Perovskite Oxide Ultrathin Nanosheet Photocatalysts with Significantly Enhanced Photocatalytic Hydrogen Evolution Activity. *Nanotechnology* **2020**, *31*, 325401. [[CrossRef](#)]
35. Nishioka, S.; Oshima, T.; Hirai, S.; Saito, D.; Hojo, K.; Mallouk, T.E.; Maeda, K. Excited Carrier Dynamics in a Dye-Sensitized Niobate Nanosheet Photocatalyst for Visible-Light Hydrogen Evolution. *ACS Catal.* **2021**, *11*, 659–669. [[CrossRef](#)]
36. Maeda, K.; Sahara, G.; Eguchi, M.; Ishitani, O. Hybrids of a Ruthenium(II) Polypyridyl Complex and a Metal Oxide Nanosheet for Dye-Sensitized Hydrogen Evolution with Visible Light: Effects of the Energy Structure on Photocatalytic Activity. *ACS Catal.* **2015**, *5*, 1700–1707. [[CrossRef](#)]
37. Greene, W.N.; Roy, N. Photocatalytic Hydrogen Evolution from Hexaniobate Nanoscrolls and Calcium Niobate Nanosheets Sensitized by Ruthenium(II) Bipyridyl Complexes. *J. Phys. Chem. C* **2009**, *113*, 7962–7969. [[CrossRef](#)]
38. Zhou, Y.; Wen, T.; Guo, Y.; Yang, B.; Wang, Y. Controllable Doping of Nitrogen and Tetravalent Niobium Affords Yellow and Black Calcium Niobate Nanosheets for Enhanced Photocatalytic Hydrogen Evolution. *RSC Adv.* **2016**, *6*, 64930–64936. [[CrossRef](#)]
39. Hong, Y.; Kim, S.-J. Intercalation of Primary Diamines in the Layered Perovskite Oxides,  $\text{HSr}_2\text{Nb}_3\text{O}_{10}$ . *Bull. Korean Chem. Soc.* **1996**, *17*, 730–735.
40. Hu, Y.; Guo, L. Rapid Preparation of Perovskite Lead Niobate Nanosheets by Ultrasonic-Assisted Exfoliation for Enhanced Visible-Light-Driven Photocatalytic Hydrogen Production. *ChemCatChem* **2015**, *7*, 584–587. [[CrossRef](#)]
41. Zhang, S.; Diehl, L.; Wrede, S.; Lotsch, B.V.; Christina, S. Structural Evolution of Ni-Based Co-Catalysts on  $[\text{Ca}_2\text{Nb}_3\text{O}_{10}]^-$  Nanosheets during Heating and Their Photocatalytic Properties. *Catalysts* **2008**, *10*, 13. [[CrossRef](#)]
42. Kurnosenko, S.A.; Silyukov, O.I.; Minich, I.A.; Zvereva, I.A. Exfoliation of Methylamine and N-Butylamine Derivatives of Layered Perovskite-Like Oxides  $\text{HLnTiO}_4$  and  $\text{H}_2\text{Ln}_2\text{Ti}_3\text{O}_{10}$  ( $\text{Ln} = \text{La}, \text{Nd}$ ) into Nanolayers. *Glas. Phys. Chem.* **2021**, *47*, 372–381. [[CrossRef](#)]
43. Karimi Estahbanati, M.R.; Mahinpey, N.; Feilizadeh, M.; Attar, F.; Iliuta, M.C. Kinetic Study of the Effects of PH on the Photocatalytic Hydrogen Production from Alcohols. *Int. J. Hydrogen Energy* **2019**, *44*, 32030–32041. [[CrossRef](#)]
44. Hota, P.; Das, A.; Maiti, D.K. A Short Review on Generation of Green Fuel Hydrogen through Water Splitting. *Int. J. Hydrogen Energy* **2022**, *48*, 523–541. [[CrossRef](#)]
45. Martín, S.S.; Rivero, M.J.; Ortiz, I. Unravelling the Mechanisms That Drive the Performance of Photocatalytic Hydrogen Production. *Catalysts* **2020**, *10*, 901. [[CrossRef](#)]
46. Davis, K.A.; Yoo, S.; Shuler, E.W.; Sherman, B.D.; Lee, S.; Leem, G. Photocatalytic Hydrogen Evolution from Biomass Conversion. *Nano Converg.* **2021**, *8*, 6. [[CrossRef](#)] [[PubMed](#)]
47. Rodionov, I.A.; Zvereva, I.A. Photocatalytic Activity of Layered Perovskite-like Oxides in Practically Valuable Chemical Reactions. *Russ. Chem. Rev.* **2016**, *85*, 248–279. [[CrossRef](#)]
48. Al-Azri, Z.H.N.; Chen, W.T.; Chan, A.; Jovic, V.; Ina, T.; Idriss, H.; Waterhouse, G.I.N. The Roles of Metal Co-Catalysts and Reaction Media in Photocatalytic Hydrogen Production: Performance Evaluation of M/ $\text{TiO}_2$  Photocatalysts ( $\text{M} = \text{Pd}, \text{Pt}, \text{Au}$ ) in Different Alcohol-Water Mixtures. *J. Catal.* **2015**, *329*, 355–367. [[CrossRef](#)]
49. Rodionov, I.A.; Maksimova, E.A.; Pozhidaev, A.Y.; Kurnosenko, S.A.; Silyukov, O.I.; Zvereva, I.A. Layered Titanate  $\text{H}_2\text{Nd}_2\text{Ti}_3\text{O}_{10}$  Intercalated With N-Butylamine: A New Highly Efficient Hybrid Photocatalyst for Hydrogen Production From Aqueous Solutions of Alcohols. *Front. Chem.* **2019**, *7*, 863. [[CrossRef](#)]
50. Kurnosenko, S.A.; Voytovich, V.V.; Silyukov, O.I.; Rodionov, I.A.; Kirichenko, S.O.; Minich, I.A.; Malygina, E.N.; Khramova, A.D.; Zvereva, I.A. Photocatalytic Activity of N-Alkylamine and n-Alkoxy Derivatives of Layered Perovskite-like Titanates  $\text{H}_2\text{Ln}_2\text{Ti}_3\text{O}_{10}$  ( $\text{Ln} = \text{La}, \text{Nd}$ ) in the Reaction of Hydrogen Production from an Aqueous Solution of Methanol. *Catalysts* **2021**, *11*, 1279. [[CrossRef](#)]
51. Rodionov, I.A.; Gruzdeva, E.O.; Mazur, A.S.; Kurnosenko, S.A.; Silyukov, O.I.; Zvereva, I.A. Photocatalytic Hydrogen Generation from Aqueous Methanol Solution over n -Butylamine-Intercalated Layered Titanate  $\text{H}_2\text{La}_2\text{Ti}_3\text{O}_{10}$ : Activity and Stability of the Hybrid Photocatalyst. *Catalysts* **2022**, *12*, 1556. [[CrossRef](#)]

**Disclaimer/Publisher’s Note:** The statements, opinions and data contained in all publications are solely those of the individual author(s) and contributor(s) and not of MDPI and/or the editor(s). MDPI and/or the editor(s) disclaim responsibility for any injury to people or property resulting from any ideas, methods, instructions or products referred to in the content.